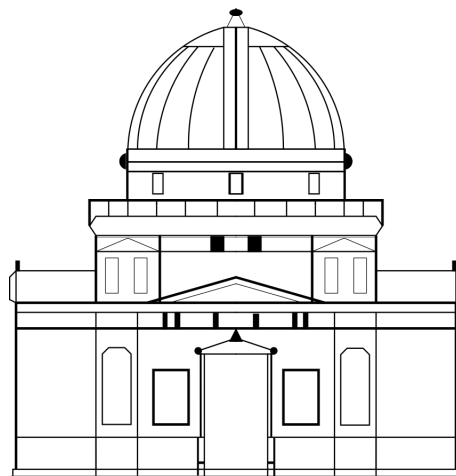


Strasbourg Astronomical Observatory



University of Strasbourg, France

Relics of Reionization in Cosmic Dawn III:
Physical properties of the remnants of photo-evaporated filaments and structures

June 11, 2024

Master's Thesis

Vishrut Bezbarua

Supervised by:
Dr. Pierre Ocvirk
Dr. Katarina Kraljic

Abstract

I use **Cosmic Dawn III**, a giant and high-resolution cosmological radiation hydrodynamics simulation to study how spatially and temporally inhomogeneous reionization impacts the baryonic and dark matter content of inter-galactic filaments. The CoDaIII simulation models an inhomogeneous reionization, follow the escape of ionising radiation from thousands of galaxies. This makes it an ideal tool for examining how ionizing sources during the Epoch of Reionization(EoR) impact the spatial and thermodynamic properties of filament environments. I compare the properties of these filaments at $z = 15$, $z = 9$, $z = 7$ and $z = 5$ to investigate the effects of ionising radiation on these filaments through the Epoch of Reionization. I develop a methodology to study the properties along and around individual filaments, and extend this methodology to the whole filamentary network contained in a sub-region of volume 2.95^3 cMpc^3 of the entire simulation box (94.43^3 cMpc^3). I observe that the thickness of the low-density filaments increase through the EoR, while the high-density counterparts develop a high-temperature envelope around them, while maintaining and relatively colder and neutral spine.

Keywords: Cosmology, Epoch of Reionization, Evolution of Galaxies, Large-scale Structures, Inter-galactic Medium, Filaments

Contents

1	Introduction	1
2	Methodology	4
2.1	Cosmological simulation : Cosmic Dawn III	4
2.1.1	Initial conditions and cosmology	5
2.1.2	Deployment	6
2.2	Filament Extraction with <i>DisPerSE</i>	6
2.2.1	<i>mse</i>	6
2.2.2	<i>skelconv</i>	6
2.2.3	Variation with Persistence Threshold	8
2.2.4	Defining a filament	9
2.2.5	Defining the filament surroundings	11
2.2.6	Categorising filaments	12
3	Analysis of individual filaments	14
4	Generalising to the entire filamentary network	17
4.1	Density distribution of the filamentary network	17
4.2	Evolution of associated properties	18
4.2.1	Neutral Fraction Properties	18
4.2.2	Thermal Properties	19
4.2.3	Baryonic density properties	19
4.2.4	Dark matter density properties	20
4.2.5	Metallicity properties	20
5	Conclusions	24

Chapter 1

Introduction

Filamentary networks stand as fundamental features of the large-scale structure (LSS) of the Universe, stretching across vast cosmological distances. Filaments can be found in multiple scales. Those evident in Fig. 1.1 reflect galaxy over-densities aligned along preferred directions, illustrating how galaxies assemble into string-like structures that underpin the cosmic architecture. These correlated structures can be seen up to billions of light years in length and are created and shaped by gravity. Just as gravity on smaller scales pulls together gas particles to make stars, and pulls together stars to make galaxies, it also pulls together galaxies and matter into patterns on larger scales. These patterns often contain large filaments of galaxies, and voids in between, and is often referred to as ‘the cosmic web’ (Bond et al. 1996, Pogosyan et al. 1998).

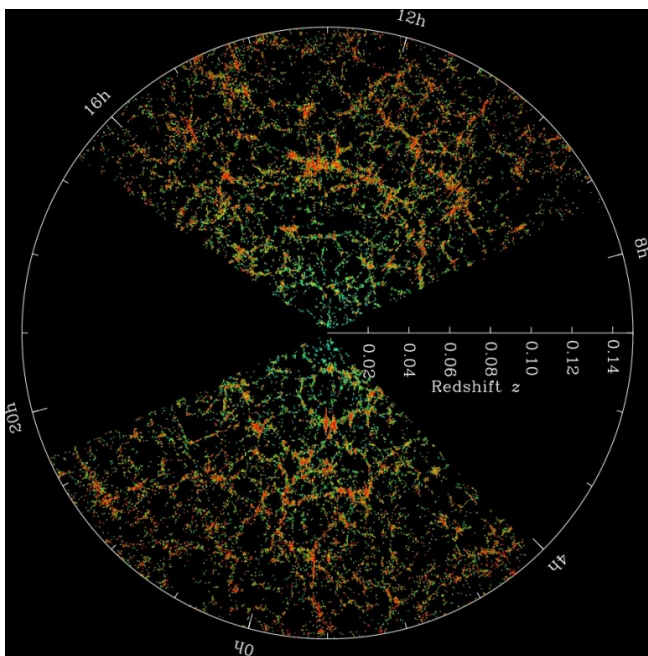


Figure 1.1: This figure shows galaxies discovered by the Sloan Digital Sky Survey (SDSS). Red points are galaxies with more red starlight, indicating older and often larger galaxies. The web-like distribution of galaxies on large scales can be seen by the eye. Figure Credit: M. Blanton and SDSS

Direct observations of the distant cosmic web are particularly difficult due to the steep decline in surface brightness with increasing redshift, rendering cold filaments exceptionally hard to detect in emission. Nevertheless, detection is not entirely impossible, as evidenced by several studies (Giavalisco et al. 2011; Ribaudo et al. 2011; Kacprzak et al. 2012; Martin et al. 2016; Gallego et al. 2018; Elias et al. 2020). These efforts often rely on techniques such as stacking or using a bright background source to enhance visibility. Filaments are commonly traced by

Although these filamentary networks are readily detectable using individual galaxies as tracers in large-sky galaxy surveys like the SDSS (York et al. 2000) and DESI (Guy et al. 2023), the gaseous component of the same are extremely faint, making them very hard to detect. Clusters of haloes form at filament intersections where, according to cosmological hydrodynamics simulations, galaxies at high redshift grow in mass and angular momentum, primarily by material transported along these filaments (Birnboim & Dekel 2003; Kereš et al. 2018, Ocvirk et al. 2018; Pichon et al. 2011; Danovich et al. 2012; Stewart et al. 2013). This makes them an interesting subject of study, given that they are key components that directly determine the birth and fate of galaxies. To better understand the role of cosmic filaments in galaxy evolution, it is crucial to obtain quantitative, direct measurements of their properties - how they are distributed in space, which parts are hotter, etc. However, the inherent faintness of these structures poses significant challenges for comprehensive observations (Kimm et al. 2018).

Lyman- α blobs (LABs) and emitters (Kikuta et al. 2019, Umedata et al. 2019), which serve as indicators of these elusive structures. On larger scales, filamentary gas can potentially be detected in the radio with the Square Kilometer Array (Kooistra et al. 2019). Lyman- α forest tomography also allows the probing of the cosmic web in the IGM, with the feasibility of observations for the Very Large Telescope investigated by Lee et al. (2014) and the European Extremely Large Telescope by Japelj et al. (2019). This will enable the detection and exploration of the full three-dimensional structure of the cosmic web.

Recent efforts to study the properties of intergalactic filaments at high redshifts were made by Ramsøy et al. (2021), where these authors utilized a cosmological zoom-in simulation of a Milky Way (MW)-mass halo, with a mass of approximately $5 \times 10^{11} M_{\odot}$ at $z = 0$, derived from the NUT suite (Powell et al. 2011) and executed with the adaptive mesh refinement (AMR) code RAMSES (Teyssier 2002). Their study focused on the properties of the main filament feeding the central halo in the redshift range $z \approx 3.5\text{--}8$, with particular emphasis on $z \approx 4$. During this period, the filament extended approximately 200 cKpc¹ on either side of the halo and did not appear to connect to any other massive object. The spatial resolution of the analyzed filament was around 1.2 cKpc, with smaller regions around embedded halos achieving a resolution of approximately 0.6 cKpc. Ramsøy et al. (2021) found that the filament could be well described by a model of an isothermal, self-gravitating, infinite cylinder (Ostriker 1964), embedded within an isothermal self-gravitating sheet that dominated the mass distribution at distances greater than approximately 15–20 cKpc from the filament axis. This description was consistent for both gas and dark matter, whose density profiles exhibited very similar shapes and widths. An accretion shock was identified around the filament, indicated by a sharp increase in gas temperature. However, the post-shock gas was observed to cool rapidly, limiting the shock width to a few cKpc.

While the analysis and results of Ramsøy et al. (2021) are extremely detailed, their focus on a single filament feeding an isolated high-redshift progenitor of a MW-mass halo raises questions about the generalizability of their findings – it remains uncertain whether their results are applicable to filaments feeding more massive halos ($M_v \gtrsim 10^{12} M_{\odot}$) as cold streams at high redshifts, given the significant mass difference. Therefore, additional studies examining filaments feeding halos of varying masses, in different environments, and at different redshifts are necessary to draw more comprehensive conclusions about the general properties of the filament population.

Through this master’s thesis, I have attempted to arrive at some general conclusions about how a filamentary network, with a variety of associated properties like temperature, neutral fraction, gas density, dark matter density, and metallicity, evolve in time, through the EoR and particularly *due to* the EoR. The EoR is a particularly important phase of cosmic history for the purpose of studying filamentary networks, because it is during this stage that the intergalactic medium goes through several transformations. This is when the Universe shifts from a cold and neutral state, to a hot and ionised one. These transformations directly impact the large scale structures, making the study of their temporal evolution quite instructive. I use Cosmic Dawn III (CoDaIII) (Lewis et al. 2022), a giant and high-resolution cosmological radiation hydrodynamics simulation, which models an inhomogeneous reionization and follow the escape of ionising radiation from thousands of galaxies. This makes it an ideal tool for examining how ionizing sources during the EoR impact the physical and thermodynamic properties of filament environments – this is in direct contrast to the uniform ionizing background implemented in Ramsøy et al. (2021). The box size of the entire simulation of 94.43^3 cMpc³, but for the purpose of this thesis, I only use a sub-region of this simulation (2.95^3 cMpc³) at four different redshifts 15, 9, 7 and 5 (roughly spanning across the EoR). Taking into account limited computational resources and short timeframe, this study serves as a good precursor to further generalisation to the other regions of the larger simulation box, which might

¹Comoving distance is a measure used to describe the separation between two points in the universe in such a way that the effect of the universe’s expansion is removed.

or might not have drastically different distribution of baryonic or dark matter density.

Chapter 2

Methodology

2.1 Cosmological simulation : Cosmic Dawn III

The Cosmic Dawn (CoDa) simulation suite uses the most powerful supercomputers in the world to simulate how galaxies form during the Epoch of Reionization, how they drive reionization, and how the rising UV background during this period then impacts galaxy and large scale structure formation in return. The simulations were performed at Oak Ridge Leadership Computing Facility (OLCF) on Titan and Summit using several in-cite allocations. They use the fully-coupled radiation-hydrodynamics code RAMSES-CUDATON ([Ocvirk et al. 2016](#)) to model a region of $64 \text{ h}^{-1} \text{ cMpc}$ using up to a trillion cells and particles. The goal of the project is to gain a better understanding of the Epoch of Reionization and its interaction with galaxy formation, and to produce, or help produce mock observables of galaxy populations for telescopes such as James Webb Space Telescope (JWST¹), as well as for the 21cm observatories such NenuFAR² and the Square Kilometer Array³.

RAMSES-CUDATON results from the coupling of the RAMSES code for N-body dark matter dynamics, hydrodynamics, star formation, and stellar feedback ([Teyssier 2002](#)), with the radiative transfer module ATON ([Aubert & Teyssier 2008](#)), which handles the radiative transfer of ionizing photons via the M1 method ([Levermore 1984](#)), hydrogen photoionization, and thermochemistry. Motivated by the important computational cost of radiative transfer, ATON module is accelerated using GPUs ([Aubert & Teyssier 2010](#)), whilst the remaining RAMSES physics run on CPUs. The performance boost thus obtained allows to run fully coupled simulations with a full speed of light, circumventing pitfalls encountered by certain reduced speed of light approaches ([Gnedin 2016](#); [Deparis et al. 2019](#)), in particular on the residual neutral fraction after overlap ([Ocvirk et al. 2019](#)).

For the most part, the code and simulation set-up are as described in [Ocvirk et al. 2020](#), but with higher resolution.

- CoDaIII uses an 8192^3 grid.
- In CoDaIII, each stellar particle receives an ionizing emissivity value based on its mass, age, and metallicity. Emissivities are pre-computed using BPASS v2.2.1 ([Stanway & Eldridge 2018](#)), considering that each stellar particle is a star cluster of about 10^4 M_\odot forming over a few Myr as in [Ocvirk et al. 2021](#).
- For a gas cell to form stars, it is not only required that it is dense enough, but also that it is cooler than $2 \times 10^4 \text{ K}$. This additional temperature threshold for star formation has been widely used in similar simulations before CoDaIII including CoDa I ([Ocvirk et al. 2016](#)) and others (e.g. [Dubois & Teyssier 2007](#)). Its physical interpretation is as follows: gas cells hotter than the threshold are so because of shocks,

¹<https://webb.nasa.gov/>

²<https://nenufar.obs-nancay.fr/en/astronomer/>

³<https://www.skao.int/en>

usually caused by supernovae, which are not favoured sites for star formation until they manage to cool back down to below the 2×10^4 K threshold.

- Upon reaching 10 Myr of age, a mass fraction $\eta_{SN} = 0.2$ of stellar particles detonates as supernovae. Each supernova event injects 51 erg of energy for every 10 solar masses of progenitor mass into its host cell (using the kinetic feedback of (Dubois & Teyssier 2007)). After the supernova event, a long-lived particle of mass $(1 - \eta_{SN}) M_{birth}$ remains. CoDaIII features the standard RAMSES chemical enrichment. 3 Metals are produced by supernovae. A fraction $y = 0.05$ of the total supernova mass is reinjected as metals. Metallicity is treated as a passive scalar, and metals are thus advected along with the gas.

For quick reference, Table 1 recaps the essential physical and numerical parameters of CoDaIII.

Table 2.1: Overview of the CoDaIII simulation.

Set-up	
Grid size and dark matter particle number	8192^3
Box size	94.43 cMpc
Force resolution	
Comoving	11.53 ckpc
Physical ($z = 6$)	1.65 pkpc
Dark matter particle mass	$5.09 \times 10^4 M_\odot$
Average cell gas mass	$9.375 \times 10^3 M_\odot$
Stellar particle mass	$11,732 M_\odot$
Star formation and feedback	
Density threshold for star formation	$50 \rho_{\text{gas}}$
Temperature threshold for star formation	2×10^4 K
Star formation efficiency, ϵ	0.03
Massive star lifetime	10 Myr
Supernova energy	10^{51} erg
Supernova mass fraction, η_{SN}	0.2
Supernova ejecta metal mass fraction	0.05
Radiation	
Stellar ionizing emissivity model	BPASS v2.2.1 binary(from Stanway & Eldridge 2018)
Stellar particle subgrid escape fraction, $f_{\text{sub esc}}$	1.0
Effective photon energy	20.28 eV
Effective H I cross-section (at 20.28 eV)	$2.493 \times 10^{-22} \text{ m}^2$
Reionization	
CMB electron scattering optical depth, $\tau_{\text{es}}(z = 14)$	0.0497
Reionization mid-point, z_{re} , 50 per cent	6.81
Reionization complete, z_{re} , 99.99 per cent	5.53

2.1.1 Initial conditions and cosmology

CoDaIII's initial conditions were constrained so as to produce facsimiles of the progenitors of the Local Group (Sorce et al. 2016) within the Constrained Local Universe Simulations (CLUES⁴) project. The cosmology used ($\Omega_\Lambda = 0.693$, $\Omega_m = 0.307$, $\Omega_b = 0.0482$, $H_0 = \text{km s}^{-1} \text{ Mpc}^{-1}$, $\sigma_8 = 0.829$, and $n_s = 0.963$) here is taken from the Planck Collaboration XVI (2014) constraints (Collaboration 2014)⁵. The initial conditions were generated at $z = 150$.

⁴<https://www.clues-project.org/cms/>

⁵these constraints are compatible with subsequent Planck publications

2.1.2 Deployment

CoDaIII was run on Summit at the Oak Ridge National Laboratory/Oak Ridge Leadership Computing Facility. It was deployed on 13,1072 processors coupled with 24,576 GPUs, distributed on 4096 nodes, and ran for about 10 days, allowing CoDaIII to reach a final redshift of $z = 4.6$, i.e. sufficiently late after overlap that one can consider reionization complete and sample well into the post-overlap phase. Snapshots were written every 10 Myr, a subset of them were used to derive the properties of the IGM in the following section. Subsequent processing of the more than 20 PB of data outputs took place at the same facility on Andes and Summit.

2.2 Filament Extraction with *DisPerSE*

The extraction of the filamentary networks is facilitated by the open-source DIScrete PERsistent Structures Extractor (DisPerSE) (Sousbie 2011; Sousbie et al. 2011). The Morse-Smale complex⁶ of the baryonic matter density field is computed using the *mse*⁷ routine of DisPerSE. This routine identifies critical points (maxima, 2-saddle points, and minima) within the 3D density cube. Integral lines connecting these critical points are then traced, following the direction of the least gradient of the density field. Filamentary structures are delineated by ascending 1-manifolds, resulting in thousands of individual segments that make up the filamentary network. Each pair of critical points (e.g. maxima–saddle) is assigned a persistence, namely a measure of how significant it is with respect to a Poisson distribution. The persistence threshold is the single parameter that determines which features are considered as noise and which robustly pertain to the topology of the underlying density field. I set a persistence threshold of 0.2, as a common value that was found to ensure that the observed skeleton is roughly in good visual agreement with the underlying gas density field, throughout the four redshifts. Although this common threshold value ensures comparability, employing distinct persistence thresholds tailored to each redshift might also be useful, potentially enabling a more precise delineation of subtle variations in the density distributions in the four different redshifts (refer to section 2.2.3, to read more about persistence threshold and how changing its value changes the outputs). The skeleton of filaments are then smoothed with the smoothing parameter (`smooth 1`).

2.2.1 *mse*

mse, the main program within DisPerSE, is a routine for analyzing and extracting Morse-smale complexes, critical points, and persistence pairs from spatial datasets. Its practical functionality encompasses the computation of filamentary structures such as arcs, as well as the identification of voids and walls within complex datasets representing cosmological or physical phenomena. At its core, *mse* operates on input data representing a cell complex defining the topology of the space under consideration. This data may include information about scalar functions sampled over the space, such as density fields or intensity values. One of *mse*'s features is its ability to extract valuable structural information while offering flexibility in output formats. By default, *mse* computes the Morse-smale complex and stores it in a format native to the program, facilitating subsequent analysis or further processing.

2.2.2 *skelconv*

⁷In the post-processing phase following the generation of the skeleton using *mse*, the `skelconv` command is utilized to refine and extract specific data from the skeleton output.

⁶<https://www2.cs.uh.edu/~chengu/Teaching/Spring2013/Lecs/Lec8.pdf>

⁷<http://www2.iap.fr/users/sousbie/web/html/index4f3e.html?category/Manual>

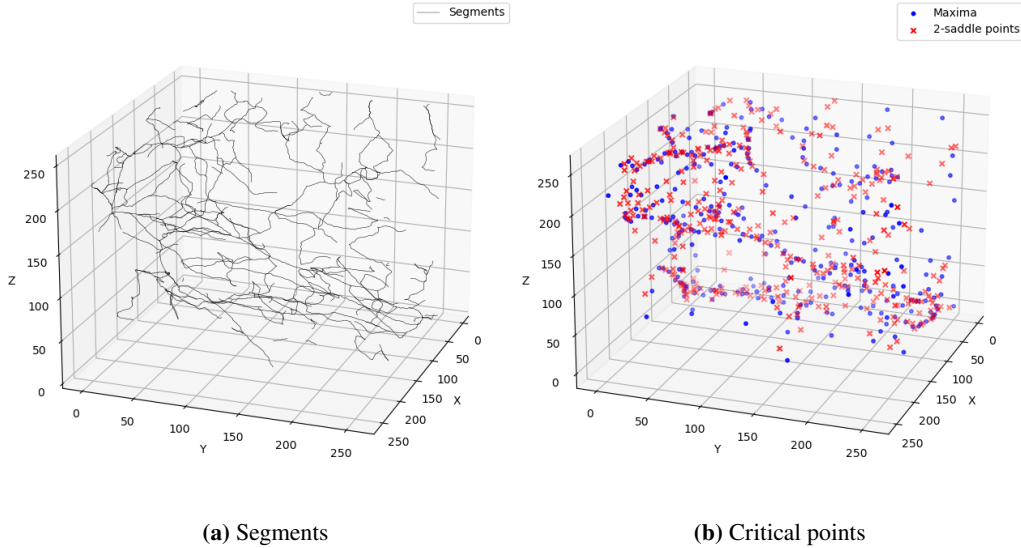


Figure 2.1: Segments and critical points (maxima and 2-saddle points) detected by DisPerSE.

With the `-smooth` parameter set to 1, the filaments are subjected to a single round of smoothing. The `-to segs_ascii` option directs the generation of an ASCII file containing segmented filament data, where each segment is defined by its constituent coordinates. Alternatively, the `-to crits_ascii` flag can be employed to generate a separate ASCII file containing critical points. These `.a.segs` and `.a.crits` files offer streamlined representations of the skeleton data. Fig 2.1a and Fig 2.1b display the results derived from plotting the output data contained in the `a.segs` (corresponding to segments) and `a.crits` (corresponding to critical points) files, respectively. Fig 2.2 shows an example of the filamentary structures of the gas and dark matter filaments as extracted by DisPerSE, plotted over the underlying DM density field. The DM field was smoothed due to it possessing a high degree of substructures, which enhances the computational demands by DisPerSE.

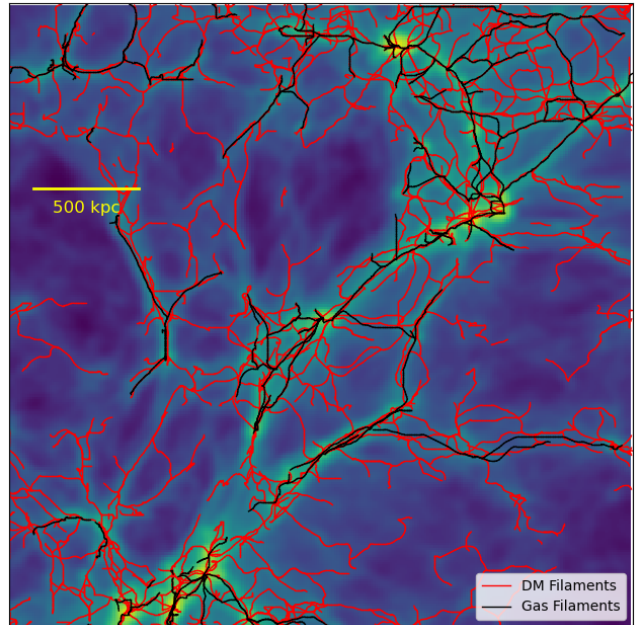


Figure 2.2: Filamentary structures of gas density field and dark matter density field plotted over a smoothed dark matter density field slab of 40 simulation cells (461.2 cKpc).

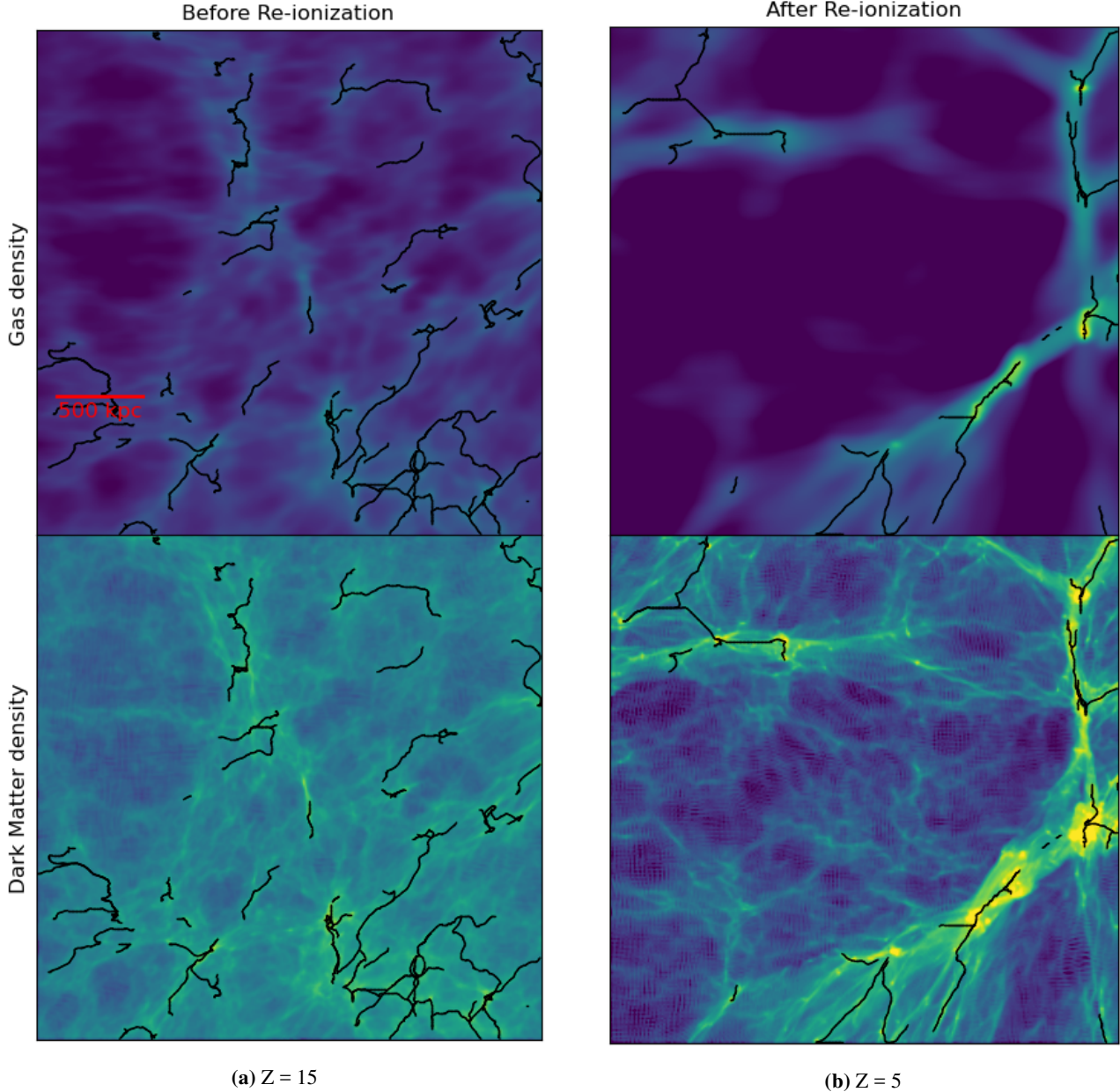


Figure 2.3: The top left image shows the projection of gas column density in a slab of size 345.9 cKpc at redshift $z = 15$, alongside the corresponding (bottom left) dark matter density projection. The set of images in the right column presents the same projections at redshift $z = 5$. The filamentary structures detected by DisPerSE using only gas density are overlaid on both gas and dark matter density maps, highlighting their significant overlap. The impact of radiation from reionization sources is evident in the gas density map on the right. The gas filaments are notably wider, and much of the diffuse structure has vanished. In contrast, dark matter, being non-collisional and influenced solely by gravity, does not exhibit these changes. The widening of the dark matter filaments is attributed to gravitational effects.

2.2.3 Variation with Persistence Threshold

To study the topology of a function, one can measure how the topology of its excursion sets (i.e., the set of points with values higher than a given threshold) evolves when the threshold is continuously and monotonically changing. Whenever the threshold crosses the value of a critical point, the topology of the excursion changes. Supposing that the threshold is sweeping the values of a 1D function from high to low, whenever it crosses the value of a maximum, a new component appears in the excursion, while two components merge (i.e., one is destroyed) whenever the threshold crosses the value of a minimum. This concept can be extended to higher dimensions. In general, whenever a topological component is created at a critical point, the critical point is labeled positive, while it is labeled negative if it destroys a topological component. Using this definition, topological components of a function can be represented by pairs of positive and negative critical points called persistence pairs. The absolute

difference of the value of the critical points in a pair is called its persistence ([Zomorodian 2009](#), [Edelsbrunner & Harer 2010](#), [Gyulassy 2009](#), [Forman 2002](#)): it represents the lifetime of the corresponding topological component within the excursion set. This concept of persistence yields a simple way to measure how robust topological components are to local modifications of function values. Indeed, noise can only affect a function's topology by creating or destroying topological components of persistence lower than its local amplitude. Therefore, it suffices to know the amplitude of noise to decide which components certainly belong to an underlying function and which may have been affected (i.e., created or destroyed) by noise. In DisPerSE, a persistence threshold can be specified (see options `-nsig` and `-cut` of `mse`) to remove topological components with persistence lower than the threshold and therefore filter noise from the Morse-Smale complex. Fig 2.4 displays the difference in the filamentary structures obtained using different persistence threshold values.

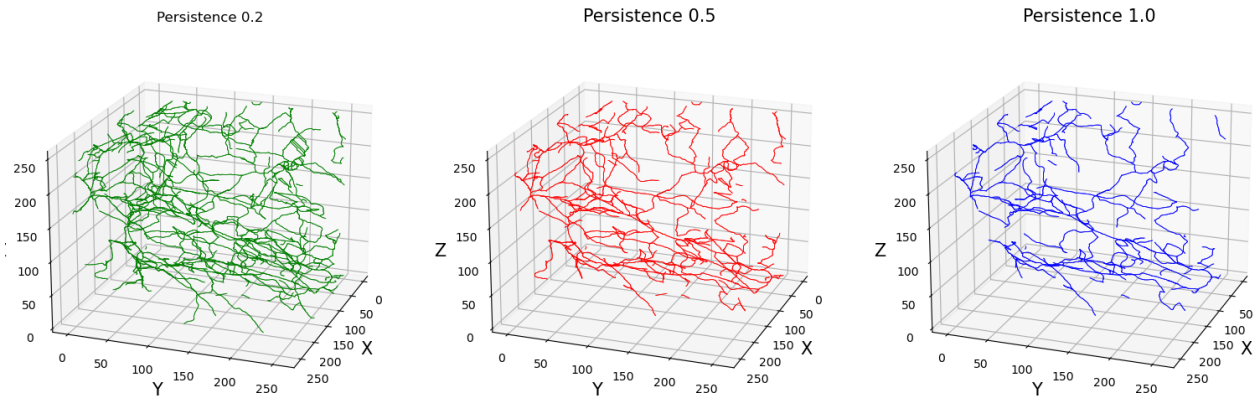


Figure 2.4: 3-D visualisation displaying the different outcomes generated due to the use of different persistence threshold values for the `-cut` parameter in the `mse` routine, plotted using `Matplotlib.pyplot`. Lower persistence gives more segments.

2.2.4 Defining a filament

In DisPerSE, a filament is a 1-dimensional structure : an ascending or descending 1-manifold. A filament consists of the set of two arcs originating from a given saddle point and joining two extrema together. Unless explicitly stated, filaments join maxima together, while void filaments or anti-filaments are the ones that link minima together. `segs_ascii` files are not arranged in a straightforward manner. They contain a list of individual segments, which join to make up filaments, while `crits_ascii` contain information on the critical points and bifurcation points only (points where filaments split into two or more).

Hence, for the purpose of obtaining a final list where each item represents a filament as a collection (or an arrangement) of unique *points*, I define a function. These unique points are basically the end points of segments, which occur twice, as two consecutive segments share a common point. This function processes the series of segments (from the `segs_ascii` file), aiming to concatenate these segments first into arcs, and then these arcs into filaments. The function first initializes empty lists for storing the unique *points* and arcs (arcs would eventually contain these *points*), then iterates through the given series of segments, checking if the end point of the current segment matches the start point of the next. If they match, the segments are appended to a temporary list; if not, this list is added to the arcs list, and a new temporary list is started. After processing all segments, any remaining points are added to arcs. The code then removes duplicate coordinates within each arc and organizes these unique arcs into a dictionary, keyed by their starting coordinates. It then attempts to concatenate arcs by checking if the start of one arc matches the start of another, concatenating them if they do, while avoiding self-concatenation, and thus forming individual filaments. This process effectively organizes and merges segments into filaments based on their spatial continuity. An example usage of the function is illustrated in Figure 2.5 and Fig 2.6. The left panel displays the filamentary structure before each filament is properly defined, while the right

panel shows the different filaments, each uniquely denoted by a different color. In both panels, the extracted and processed filamentary structure is overlaid on the underlying gas density field that it is intended to trace. Additionally, each end-point of a segment also has a density value, corresponding to the value of the function at that point. These densities are also grouped together with the coordinates of the individual points of a filament. This helps us treat specific regions of a filament(s), depending on the density of that region, to see if the variation of density along the filament has consequences in its environment in terms of other physical properties like temperature, ionization fraction, metallicity, etc (see Section 4).

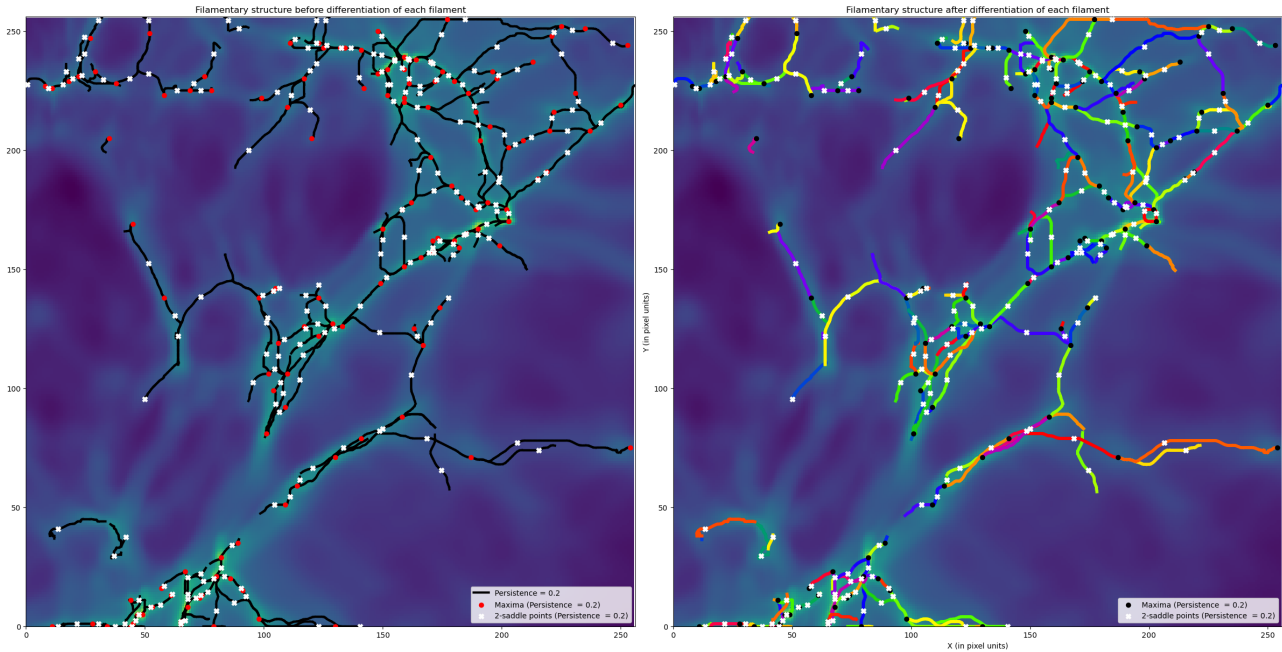


Figure 2.5: *Left panel:* Critical points and filaments hitherto undifferentiated. *Right panel:* Processed filamentary structure, with each filament uniquely colored and corresponding critical points indicated. The filamentary structures are overlaid on the underlying gas density field to illustrate the tracing accuracy.

This methodology not only facilitates the identification of filaments but also enables us to pinpoint potential filaments of interest. Fig 2.5 shows the difference between two cases, one with the undifferentiated network, and the other with individual filaments. Filaments now bear a distinctive index, affording us the opportunity to assign them a "name and significance". This not only streamlines the process but also imbues each filament with a distinct identity, potentially revealing its significance upon initial inspection across various property maps. An example application of this method can be seen in section 3, where one filament in each redshift is selected, which is followed by a characterisation of their environments in terms of different associated properties.

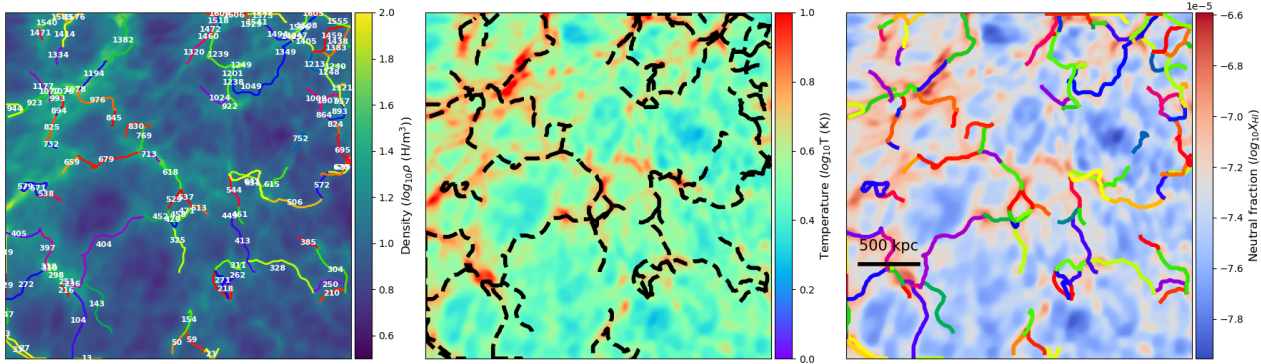


Figure 2.6: *First panel:* A projection of a 20 cells thick (230.6 cKpc) slab of density field. The filamentary structure plotted over it, each filament having a unique index. *Second panel:* A slice of temperature map, through the middle of the slab considered for the density field. The filamentary structures are overlaid on the underlying temperature field. The filaments clearly are hotter than the surroundings. *Third panel:* A slice of neutral fraction map, through the middle of the slab considered for the density field. The filamentary structure plotted over it. The filaments clearly are more neutral than the surroundings. All the maps are from $z = 15$ (before reionization).

2.2.5 Defining the filament surroundings

Once I know what are the coordinates of each point of a filament, and what is the baryonic density of the corresponding regions, the next step is to characterise the environments of these filaments. This involves profiling the regions around filaments for different properties. The core of the data processing required to implement this lies in iterating through each point in a filament, for which the function identifies the next and previous points to compute the direction vector, which helps in determining the orientation of the filament at each point. The function then defines the range for possible indices within a specified radius, R_{max} , for the x, y, and z coordinates. Using these ranges, a meshgrid is created, producing a set of points around each filament point. The points in the meshgrid are then interpolated using interpolation functions. These functions retrieve interpolated values from the data cubes for various properties: baryonic density, dark matter density, temperature, neutral fraction, ionization fraction and metallicity. The function then calculates the radial distance ('r') from the filament to each interpolated point, and filters these points to retain only those that are lie on a "perpendicular plane" (with thickness less than 0.7 cells (= 8 cKpc)), and within the radius R_{max} .

For each filtered point, the function computes the properties mentioned above. The median of these properties are taken within defined radial ranges, converting radial distances to comoving kiloparsecs (cKpc) for meaningful interpretation. The median, 25th percentile, and 75th percentile values for each property within these ranges are determined, providing information about the spread of the data.

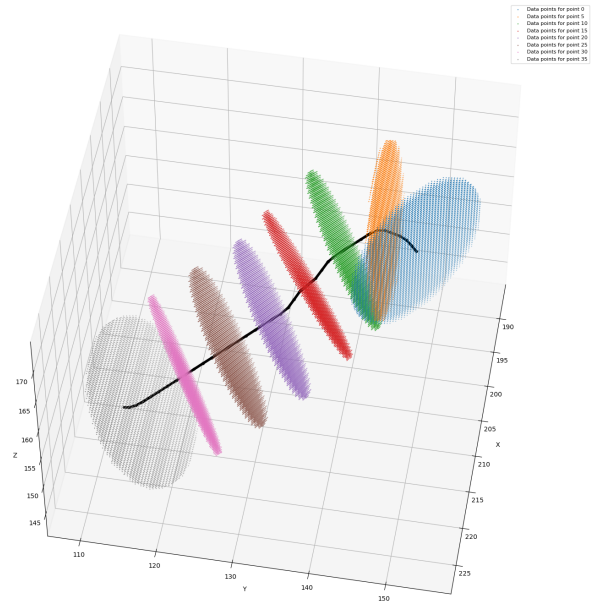


Figure 2.7: An example filament with perpendicular planes defined at specific points along the filament. These planes are oriented perpendicular to the direction of the segment connecting the point with the next point, or the previous point if the point is at the end of the filament.

2.2.6 Categorising filaments

In order to generalize the properties from the level of an individual filament, to the filaments of the entire data cube being utilised, I divided all the filaments into different parts, based on bins of density that those parts of the filaments occupy. I selected five density bins in increasing order, as shown in Table 2.2. The motivation behind this categorisation is that different filament regions, varying in density, show differences in other properties, be it in terms of temperature or metallicity content, which is something that can be already observed in the maps. Each density bin now contains, not individual filaments, but parts of them which fall into those bins. Consequently, for a given part of the filament, I acquire as many radial profiles for a given property, as there are points *in* that part. Let's call these parts "chunks", to avoid any misunderstanding.

Bin no.	$\log_{10}(\rho_{gas} \text{ in H/m}^3)$
1	0 - 0.25
2	0.25 - 0.5
3	0.5 - 0.75
4	0.75 - 1
5	1 - 1.5

Table 2.2: Bin numbers and their corresponding density ranges

To generalize this information, I follow a two-step process:

1. Considering all points in a chunk.

- Around each point in a chunk, I create distance bins up to a maximum radius R_{\max} of 15 simulation cells. Each cell is 11.53 cKpc, resulting in a total distance of 172.95 cKpc.
- R_{\max} is divided into 15 bins. For each distance bin, I compute the median value of the property of interest.
- This calculation is repeated for all points in the chunk, resulting in a set of median values for each distance bin.
- The median of these median values for each distance bin is then taken, yielding a single median profile for the chunk.

2. Considering all chunks in a density bin.

- I aggregate these median profiles by calculating, *again*, the median across all chunks within the same density bin. This yields a unified profile that represents the median conditions across different chunks for each density bin.

In summary, this process results in one median radial profile for a given property, for each density bin, at each redshift. For instance, if we aim to analyze the temperature distribution around the filamentary network at redshift 15, this approach generates five median temperature profiles—one for each of the five density bins. Each profile provides insight into how temperature varies around typical regions within the network corresponding to each density bin.

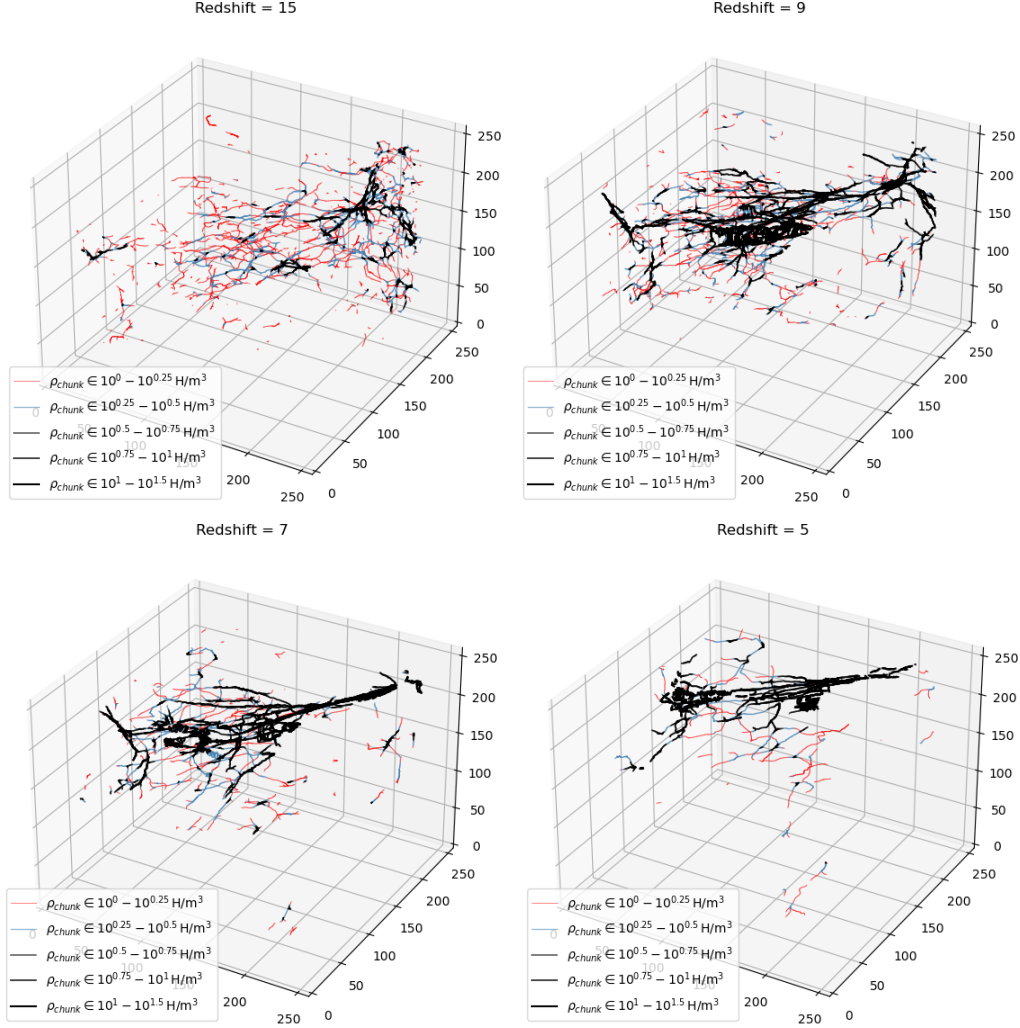


Figure 2.8: The filamentary structure in each redshift, divided into bins of density in increasing order. It's apparent that it is the same superstructure that is moving across the subcube with increasing time (decreasing redshift). The high density regions become more solidified in shape, and the low density (diffuse) counterparts slowly disappear.

Some precautions were also taken to avoid sampling points too close to the edges (or sides) of the data cubes, by making sure that I only consider regions which are atleast 20 cells away from the sides of the data cubes, the outcome of which can be seen in Fig 2.8 – all the filamentary networks stay away from 20 cells of each side of the corresponding data cube. That doesn't impact the accuracy of my results in a drastic way, as each density bin still amounts to hundreds of chunk pieces, all of which are considered before attributing a central tendency to the filaments' and their surroundings' properties. I also make sure to not sample points which might be too close to a halo region, by imposing an upper temperature limit criterion of $10^{4.5}$ K (a value chosen upon a deeper inspection : temperature profiles prior to the calculation of the final median temperature profile had shown some which were "outliers", as in, they showed enormously higher temperature values than the rest. These anomalies were likely due to regions near halos being inadvertently included.), as our objective is to only focus on regions of the filaments which lie in between these haloes.

Chapter 3

Analysis of individual filaments

Before generalizing my analysis to the whole filamentary networks detected by DisPerSE, I first test my methodology on four visually selected filaments, from the four different redshifts. These filaments are chosen based on multiple criteria to ensure their suitability for preliminary analysis – they are relatively isolated, meaning they are not in close proximity to halos, and they exhibit a relatively straight structure in three dimensions. At lower redshifts, I focused on filaments that showed well-defined temperature envelopes. To maintain consistency across different property measurements, the plots have been scaled uniformly from left to right. This standardization explains why the temperature profiles for the filament in redshift 15 are not visible (first plot of the third row). By focusing on these specific filaments, I aim to observe preliminary patterns and behaviors that can guide further studies. This approach helps me refine my methods and identify any adjustments needed before applying the analysis to the complete filamentary networks. The filaments plotted over the maps of different properties in fig 3.1 and the profiles in 3.2 correspond to each other.

Here are some comments on the obtained results about the four filaments in the four different redshifts:

- The gas density profiles from each redshift share a similar structure : regions closer to the filament are denser, as one might expect and the density gradually decreases as we go radially away from it. The extreme ends of the filament are also denser than the regions between them.
- ρ_{DM} profiles roughly share a similar structure but with more irregularities than their ρ_{baryon} counterparts. Dark matter forms clumps, unlike baryonic matter which interact via forces also other than just gravity.
- The temperature profiles for the filament from redshift 15 are not visible in the plot because all the four plots have been made to have the same upper and lower bounds of temperature values, and the first filament just happens to be much colder than the common value for the lower bound, which can be verified using the temperature maps in Fig 3.1. Some regions of the filaments also show up peaks of high temperature slightly away from their central axes.
- The filament spines are relatively more neutral than their surroundings, which progressively decreases as we go away from it.

From the plots presented, it is not feasible to draw definitive conclusions regarding the evolution of filament properties through the EoR. The filaments analyzed are not identical structures persisting through time and space; rather, they are distinct entities at each observed redshift. Consequently, any perceived trends or patterns in their evolution may be incidental, rather than indicative of genuine developmental processes.

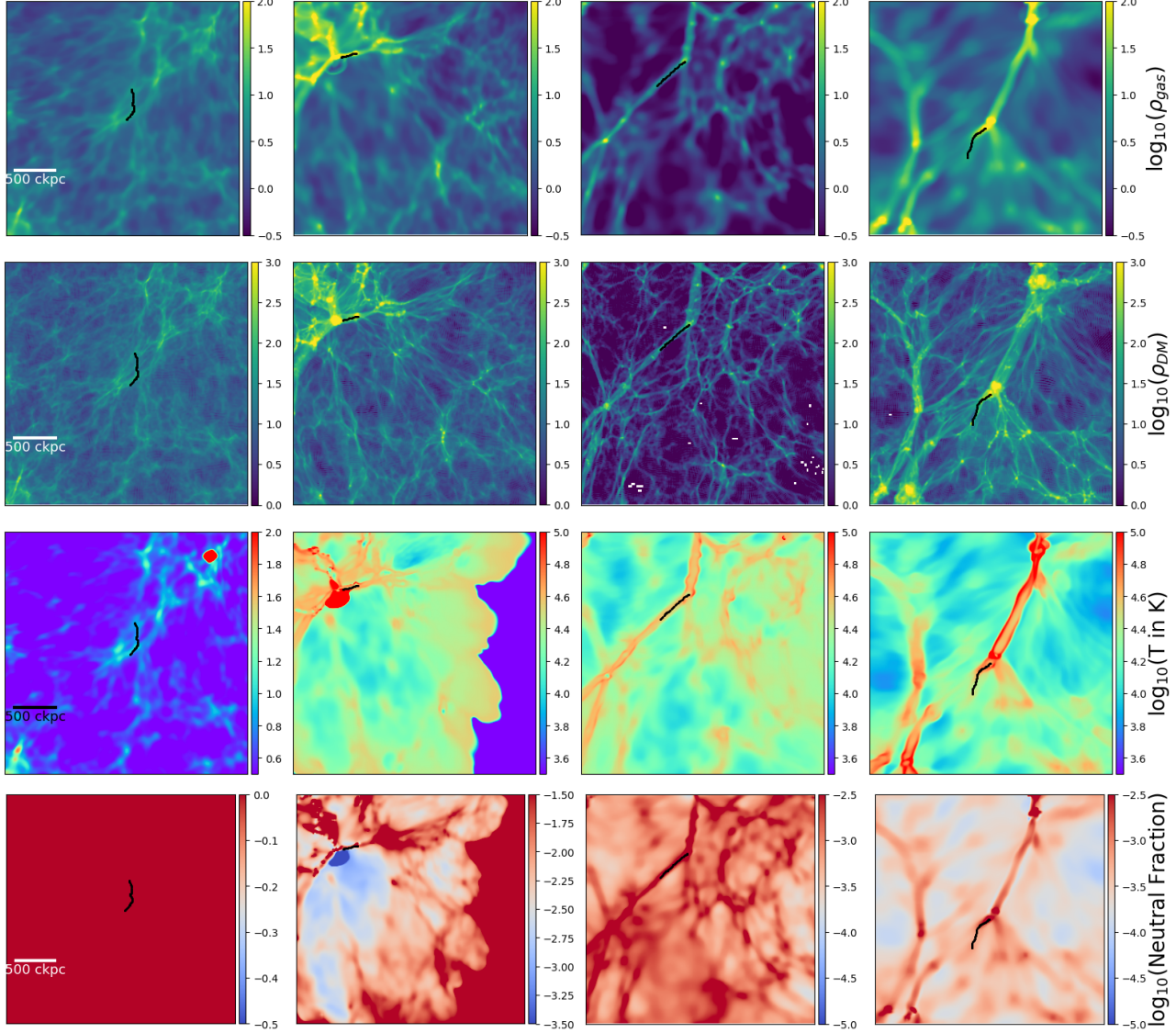


Figure 3.1: Selected filaments at $z = 15$ (1^{st} column), $z = 9$ (2^{nd} column), $z = 7$ (3^{rd} column), and $z = 5$ (4^{th} column): The first row shows baryonic (gas) density projections, the second row shows dark matter density projections, the third row shows temperature projections, and the fourth row shows neutral fraction projections. At redshift 15, the IGM is mostly neutral except in dense star-forming regions, evident from the blue region in the last row's first plot corresponding to a hot supernova event. At redshifts 9, 7, and 5, the filaments exhibit increased temperature and varying degrees of neutrality, with particularly high temperatures observed around filaments at redshifts 7 and 5.

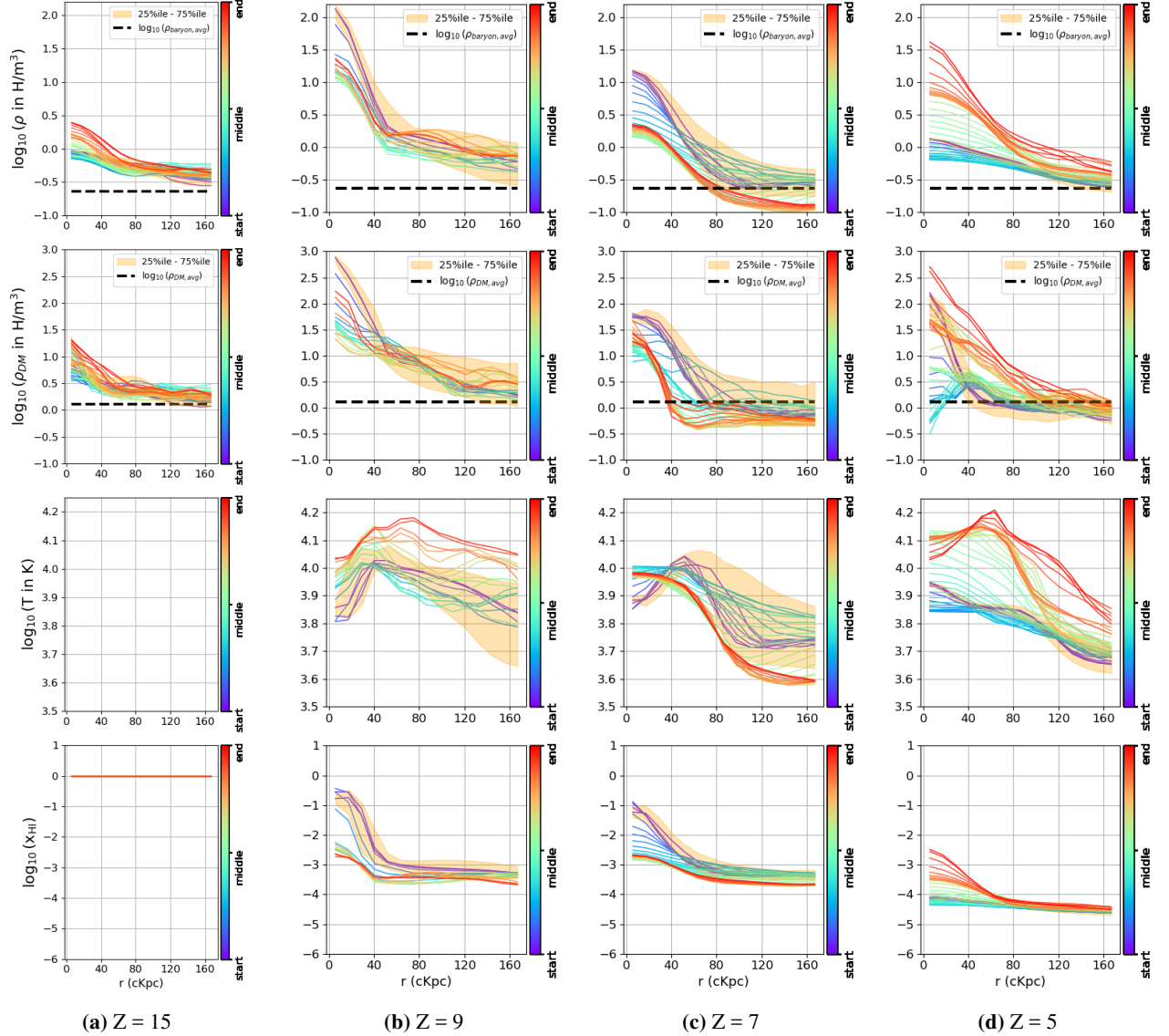


Figure 3.2: First row: Baryonic (gas) density profiles from different parts of a filament at redshifts 15 (a), 9 (b), 7 (c), and 5 (d). Second row: Dark matter density profiles from different parts of a filament at redshifts 15 (a), 9 (b), 7 (c), and 5 (d). Third row: Temperature profiles from different parts of a filament at redshifts 15 (a), 9 (b), 7 (c), and 5 (d). Fourth row: Neutral fraction profiles from different parts of a filament at redshifts 15 (a), 9 (b), 7 (c), and 5 (d).

Chapter 4

Generalising to the entire filamentary network

In this section, I take into account the four complete filamentary networks extracted by DisPerSE in the four redshifts 15, 9, 7 and 5, with a fixed persistence threshold of 0.2, to derive general conclusions regarding the transformations that the filamentary networks undergo throughout, and as a result of, the EoR. I have analysed the evolution of six properties associated with the networks : baryonic (gas) density, dark matter density, temperature, neutral fraction, ionization fraction and metallicity.

4.1 Density distribution of the filamentary network

I examine the distribution of the baryonic density of the filamentary networks in the four redshifts, to see noticeable differences in their relative abundance over time, as shown in Fig 4.1. A notable trend is observed : the denser regions of the filamentary network become more and more abundant with decreasing redshift. This trend suggests that, as the Universe evolves, gravitational forces cause filaments to become more pronounced and denser over time. Quantitatively, the analysis reveals significant changes in the density distribution of filamentary structures: **Bin 5** (highest density) experiences an increase of 266.85%. **Bin 4** sees an increase of 157.65%. **Bin 3** shows a decrease of 63.42%. **Bin 2** exhibits a decrease of 82.96%. **Bin 1** (lowest density) records a decrease of 85.40%. These trends reflect the fundamental process of structure formation in the Universe, where as high-density regions continue to accrete material and merge, they dominate the matter distribution while voids expand and become more dilute due to the overall expansion of the universe, further enhancing the disparity in density distribution over cosmic time. Fig

4.2 presents a comparison of the density distribution of the chunks within the five density bins against the density distribution of the entire filamentary structure detected by DisPerSE. This is further juxtaposed with the background density distribution of the entire intergalactic medium (IGM) considered, with a volume of approximately 3^3 cMpc^3 . This figure is crucial for understanding the rationale behind the selection of the density bins. Bin 1, representing the lowest density, is still above the average baryonic density of the universe, while Bin 5, representing the highest density, remains below the threshold required for halo formation.

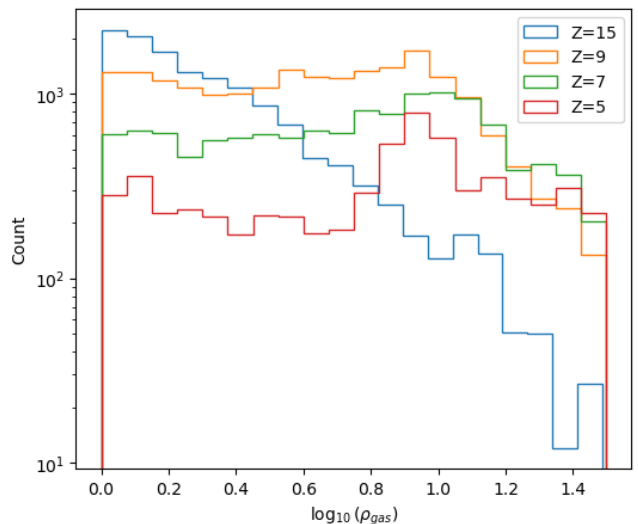


Figure 4.1: Histogram of density distributions of filamentary networks within the ranges set by the lower limit of the lowest density bin and the upper limit by the highest density bin, at different redshifts.

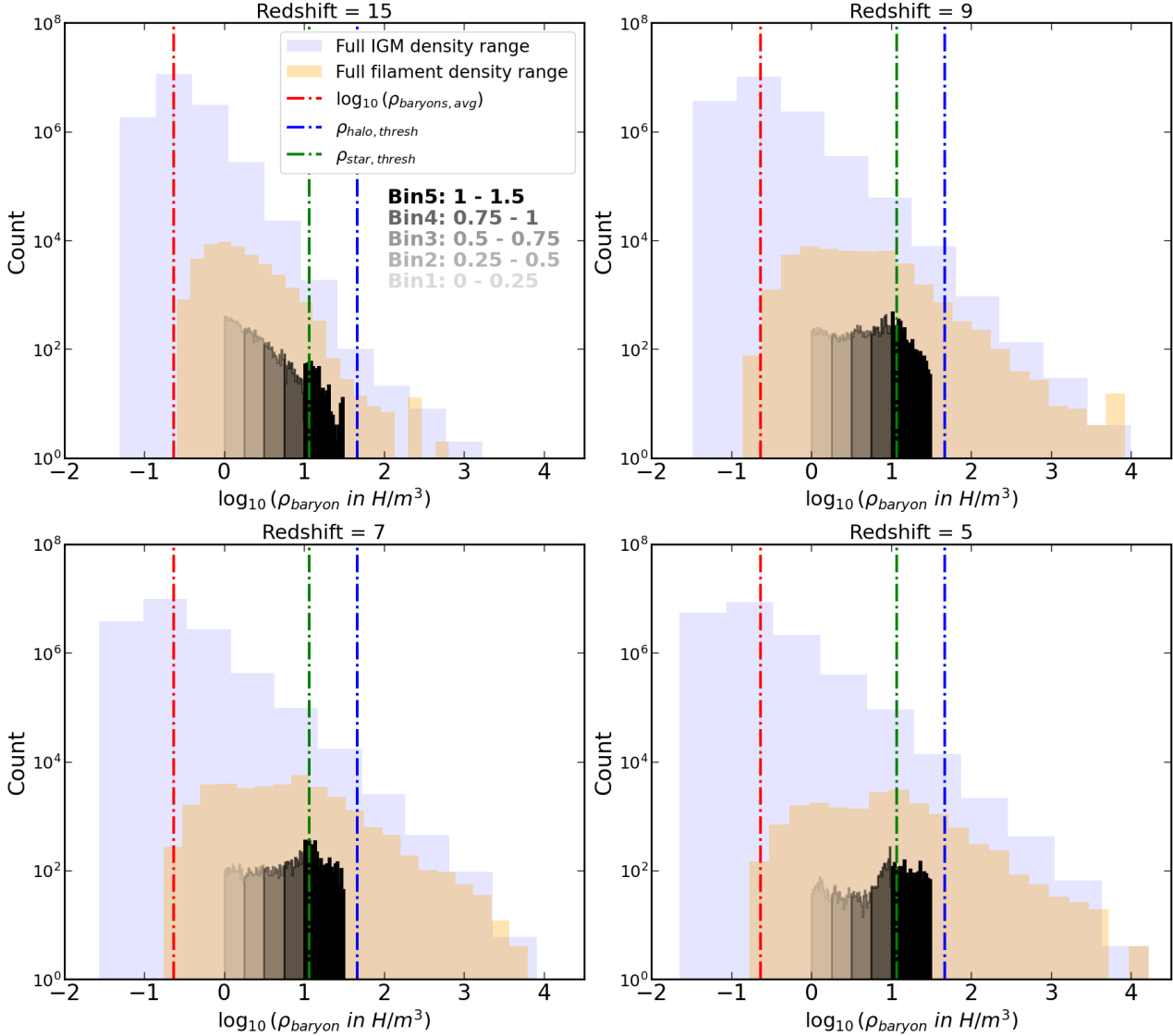


Figure 4.2: Frequency histograms representing density chunk distributions juxtaposed against all DisPerSE-detected segments, covering the full density range. The red vertical dotted lines represent the average cosmological baryonic density in logarithmic scale, $\rho_{baryon,avg}$. The blue dotted lines represent logarithmic value of the conventional threshold density for formation of haloes, which is 200 times the average cosmological baryonic density, $\rho_{baryons,avg}$. The green dotted lines represent logarithmic value of the conventional threshold density for formation of stars, which is 50 times the average cosmological baryonic density, $\rho_{baryons,avg}$.

4.2 Evolution of associated properties

In this section, I present my findings on how the different properties associated with the filamentary network evolve through the EoR, how they co-evolve with their surrounding environments and how radiative feedback from ionizing sources during the Epoch of Reionization (EoR) impacts their dynamics.

4.2.1 Neutral Fraction Properties

(3rd row, Fig 4.3) : Neutral fraction profiles for all density bins, except the highest density bin, show close-to-absolute neutrality at $z = 15$. The highest density bin exhibits a lack of neutrality likely due to the most dense regions of the filamentary networks being in proximity to ionising sources.

At $z = 9$, an overall decrease in neutrality across density bins can be observed, although the most dense regions happen to be the most ionised (least neutral). This is due to the fact that at $z = 9$, the inter-galactic medium is

still in the process of transitioning from a neutral state to an ionized one, and ionization fronts are in the process of expanding out into their neutral surroundings. Ionizing sources are produced at the densest regions of the filamentary network, making those dense regions of the filament the first to receive the effect of the ionizing fronts. That leads to an inside-out ionisation process, where the underdense regions of the IGM still remain relatively neutral, until the ionization fronts reach them.

By $z = 7$, the IGM has evolved to a near-uniformly ionized state, creating a background where ionizing photons are more pervasive. This environment allows gas density to become the primary factor influencing the neutral fraction ($x_{\text{HI}} \propto \frac{\rho_{\text{gas}}}{\rho_{\text{radiation}}}$). As a result, the reionization process shifts to an outside-in pattern, where less dense regions, which are less shielded and thus more exposed to ionizing photons, become the most ionized. This fundamentally changes the dependence of the neutral fraction on density, reversing the initial trend and making the least dense regions the most ionized. The overall decrease in neutrality stays consistent, and repeats at $z = 5$ as well. A persistent observation across $z = 9$, $z = 7$, and $z = 5$ is that the spines of the filaments, regardless of their density, maintain a higher degree of neutrality compared to their surroundings.

4.2.2 Thermal Properties

(5th row, Fig 4.3) : The temperature profiles show an overall increasing trend as a function of decreasing redshift, indicating the ionizing sources during EoR slowly heating up the cold Universe.

At $z = 15$, the highest density bin can be distinctly identified from the others, as it exhibits a temperature profile several orders of magnitude higher than those of the lower density bins, extending up to a distance of about 130-140 cKpc from the filaments. This is again due to the same fact expressed in the case of neutral fraction, that the densest regions of the filamentary network are physically closer to the ionizing sources, which are typically located in areas that have reached the critical density for star formation. The abrupt drop in the temperature profile for the highest density bin can be attributed to the expanding ionizing bubbles, which have not yet fully diffused into the surrounding regions. At $z = 9$, the lower density regions of the filamentary network begin to heat up, and by $z = 7$, they become as hot as the most dense regions. This trend continues, and by $z = 5$, the filaments reach their peak temperatures, becoming the hottest ones observed across all redshifts.

(6th row, Fig 4.3): In this section, I focus on a specific temperature range of $10^{3.5} - 10^{4.5}$ K to better highlight the peaks in the temperature profiles. The temperature peaks have been marked with the dotted vertical lines, only for the highest density bin, as it is the only bin consistently having these peaks in their profiles across redshifts. These peaks begin to appear as early as $z = 9$, within a distance of less than 40 cKpc from the filament spines. By $z = 5$, the peaks have shifted, occurring at distances greater than 40 cKpc from the filament spines. This shift indicates the outward expansion of heated envelope around the high density filaments as reionization progresses.

4.2.3 Baryonic density properties

1st row, Fig 4.3 : Gas density profiles across redshifts, follow similar trends. The filaments are denser than their surroundings. At $z = 15$, the profiles begin to flatten out between 40-80 cKpc from the filament axes. With decreasing redshift, the first three low density profiles progressively flatten, indicating thickening of filaments. Although it is difficult to attribute a certain thickness to the filaments, the trend, however, stays consistent with the outward movement of high temperature regions, inferred from the temperature profiles (5th row, Fig 4.3) as well as from Fig 4.4, where the gas density profiles for identical density bins at redshifts 15 and 5 are plotted sequentially to facilitate a comparison of the degree of expansion in both low and high density regions of the networks before and after reionization.

4.2.4 Dark matter density properties

The dark matter density profiles follow similar trends as the baryonic density counterparts. While the baryonic density profiles remain relatively stable, noticeable differences emerge in the dark matter profiles of the higher density bins (Bins 4 and 5) compared to the lower density bins (Bin 1, 2 and 3). Specifically, the dark matter density (ρ_{DM}) in the bins 1, 2 and 3 begins to decline to the average dark matter density ($\rho_{DM,avg}$) within a range of 40-80 cKpc from the filament axes. In contrast, the higher density regions exhibit a broader width, with their dark matter density dropping to $\rho_{DM,avg}$ only beyond 100 cKpc from the filament axes. This indicates that the higher density filaments possess a thicker structure, distinguishing them from their lower density counterparts. This is quite likely a direct consequence of the hierarchical growth of structures in Λ CDM cosmology, with dark matter, by design, accreting matter only through gravitational forces.

4.2.5 Metallicity properties

Metallicity values in the range of 10^{-5} to 10^{-6} indicate star formation activity in the nearby regions. I observe that only the highest density bins exhibit metallicity profiles within this range, and this is evident only at redshifts $z = 9$, $z = 7$, and $z = 5$. The absence of metallicity profiles at $z = 15$ can be attributed to the nascent stage of star formation at this early epoch. At $z = 15$, star formation has not yet become widespread within the data cube, and most of the intergalactic medium (IGM) remains unaffected by star formation. Consequently, when median metallicity profiles are calculated, the majority of the regions considered still have zero metallicity, likely resulting in an overall lack of detectable metallicity in the data at this redshift.

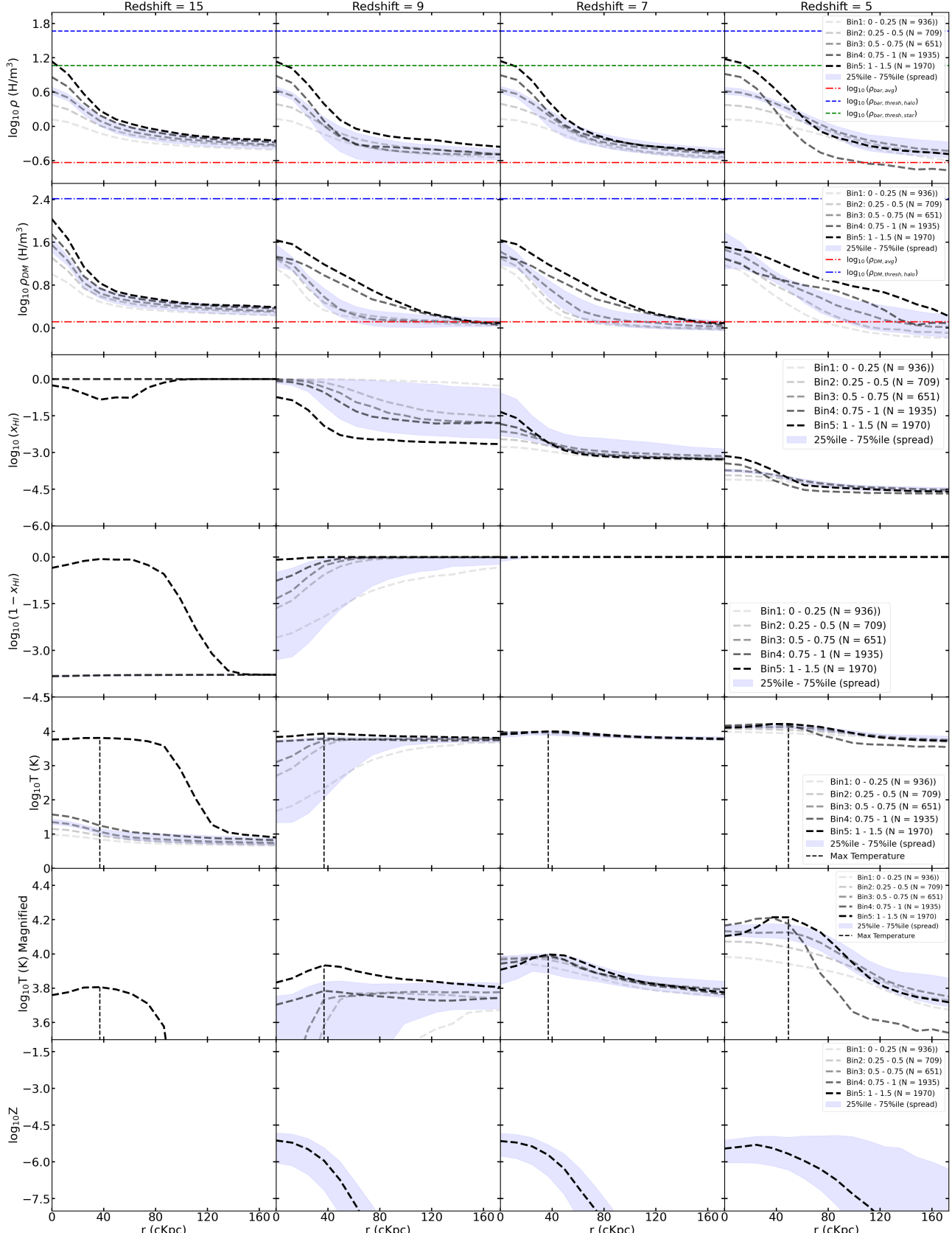


Figure 4.3: Gas density profiles (first row), Dark matter density profiles (second row), neutral fraction profiles (third row), ionisation fraction profiles (fourth row), temperature profiles (fifth row), a magnified version of the same temperature profiles (sixth row), and metallicity profiles of filaments in the simulations at redshifts 15, 9, 7 and 5. The radius represents the cylindrical radius, perpendicular to the filament. The multiple lines in each panel represent profiles from filaments with different densities, with lower density parts indicated by more transparent lines. The red horizontal dotted lines represent $\log_{10}(\Omega_{DM}/\Omega_b)$. The black vertical dotted lines in the temperature profile panels indicate the temperature maxima existing within 172.95 cKpc from a typical filament region, the density of which ranges from 10 H-atoms/m^3 to $31.62 \text{ H-atoms/m}^3$. The blue line in the first row denotes the threshold density value for halo formation.

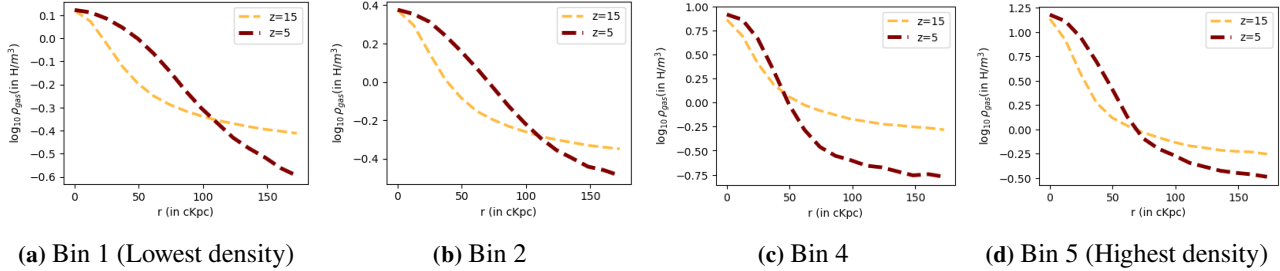


Figure 4.4: Gas density profiles for the 1st, 2nd, 4th and 5th density bins in redshift 15 and 5 (before and after reionization), to illustrate swelling of the filaments. The lower density regions of the filaments appear to expand to a greater extent over time than their higher density counterparts.

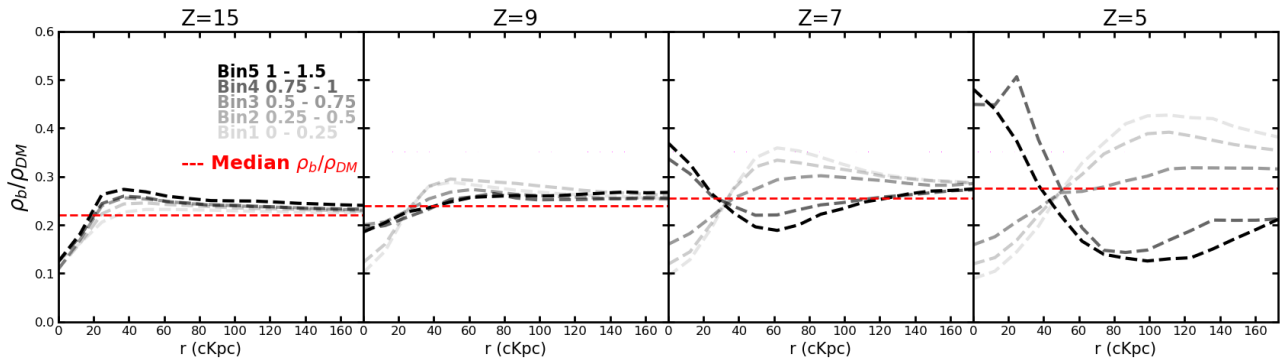


Figure 4.5: Median ρ_b/ρ_{DM} profiles from filament regions belonging to different density bins. The bins have been denoted in the units of $\log_{10}(\rho_b \text{ in } \text{H}/\text{m}^3)$. The red dotted lines denotes the ratio of median baryonic and dark matter density of the data cubes used depending on the redshift, which is seen to slowly increase with decreasing redshift. The four cells from left to right represent the profiles from $z = 15$ (before reionization) to $z = 5$ (after reionization).

In Figure 4.5, I observe the evolution of the baryon-to-dark matter density ratio ρ_{baryon}/ρ_{DM} across different redshifts and density bins. The behavior can be broadly categorized into two distinct patterns: one for density bins 1, 2, and 3, and another for density bins 4 and 5.

Bins 1, 2, and 3: Relative deficit of baryons in filament spines

For Bins 1, 2, and 3, the ρ_{baryon}/ρ_{DM} profiles exhibit similar trends across all redshifts. As redshift decreases, the ratio peaks at gradually increasing magnitudes and at progressively greater distances from the filament spines. This indicates that for regions of the filamentary network corresponding to the first three bins, baryonic matter becomes more prominent relative to dark matter at larger distances from the filaments, as the Universe evolves. However, closer to the filament spines, the ρ_{baryon}/ρ_{DM} ratio consistently shows a suppression, suggesting that dark matter is more concentrated in these regions compared to baryonic matter.

Bins 4 and 5: Transition and Increasing Ratios

Bins 4 and 5, however, display a different evolution. At redshift 15, the $\frac{\rho_{gas}}{\rho_{DM}}$ values in these bins follow a trend similar to that of the lower density bins. But as time progresses, a significant shift occurs. By redshift 7, the ratios for Bin 4 and 5 no longer show a peak, but on the contrary, they show a minimum, at around 60 cKpc from the filament axes. At redshift 5, the ρ_{baryon}/ρ_{DM} values for Bins 4 and 5 continue to evolve distinctly. Within the filament cores, the ratio reaches values close to 0.5, indicating a higher concentration of baryonic matter relative to dark matter. But beyond the core regions, between 40-60 cKpc for both Bin 4 and Bin 5, values drop below the

median values of this ratio in the selected subregion of the simulation. This suggests that at $z = 5$, as we go further from the filament cores, we have a lower relative density of baryonic matter compared to dark matter.

In the lower density bins (Bins 1, 2, and 3), the suppression of the ratio near filament cores suggests a gravitational influence where dark matter dominates. In contrast, the higher density bins (Bins 4 and 5) show a progressive increase in the baryonic matter concentration within the filaments over time. For each redshift, ρ_{baryon}/ρ_{DM} converges to the median value of the ratio, at larger distances from the filaments, even more so for the lower density density bins.

Chapter 5

Conclusions

In this work, I have utilised **Cosmic Dawn III**, a giant high-resolution cosmological simulation of the Epoch of Reionization, to characterize the evolution of inter-galactic filaments embedded in the simulation. The primary objective of this project is to see how ionizing radiation from the stars and galaxies through the EoR impact the physical and thermodynamic properties of these filaments, the understanding of which is of utmost importance, given the role it plays in feeding mass and angular momentum to all galaxies.

However, certain caveats should be considered before interpreting these results. The data cubes utilized thus far approximate a volume of 3^3 cMpc^3 , which is $(1/32)^3$ of the original box volume of the simulation, approximately 94^3 cMpc^3 . This scale reduction limits the generalizability of my findings to regions that might exhibit significantly different density distributions. Additionally, further improvements could be made by refining the exclusion of filament segments that are too close to, or within, galactic haloes, through the introduction of a distance criterion in addition to the existing temperature criterion. While these near-halo detections could potentially affect the results, efforts have been made to mitigate this issue by ensuring that the density bins used are well removed from the halo formation density threshold, which is 200 times the cosmological average baryonic density, $\rho_{b,avg}$. With these caveats in mind, my conclusions can be summarised as follows:

- Lower density parts of the filament decrease in number as a function of time, whereas the higher density regions become more frequent. While gravity plays a role in assembling lower density structures into higher density ones, in accordance with the hierarchical formation of structure in ΛCDM cosmology, radiation pressure from ionising sources might also be playing a part in erasing some of these low density structures.
- Temperature of the IGM along and around the filaments increases as a function of time, while in fixed time, the filaments themselves are hotter than their surroundings. High density parts of filaments are also more likely to form envelopes of high temperature around them with the colder central axis (see row 6 of figure 4.3). Lower density parts do not show such peaks in temperature. The distance of these temperature peaks from the central axis of the filaments increases as a function of time, indicating outward movement of the high temperature envelope. The peaks get hotter as a function of time.
- Neutral fractions of all filament regions, and their corresponding environments, decrease as a function of time, indicating radiation sources ionising the IGM, including the filaments. By $z = 7$, the IGM becomes mostly ionized, making ionizing photons quasi-uniformly spread. This causes gas density to be the main factor affecting the neutral fraction. Less dense regions become the most ionized, reversing the initial trend where denser regions were more ionized. The spines of filaments, regardless of their density, remain more neutral than their surroundings across redshifts.
- The ρ_{baryon}/ρ_{DM} ratio converges to the median value for each redshift as the radial distance from the filaments increases. Additionally, the profiles for the three lowest density bins exhibit a decrease in this ratio closer to the

filament cores. The complex trends with mass and evolution challenge a simple interpretation and require a more in-depth study.

- It appears that only the highest density bin experiences significant influence from nearby star formation, which can be inferred from the metallicity profiles. Stellar feedback likely contributes to the formation of the temperature envelopes observed. The exact mechanisms behind the temperature envelopes are not entirely clear, particularly whether it results solely from radiation from these stars or if supernova feedback also plays a role. However, it is likely that radiation is the primary factor, since high-resolution and idealized simulations without supernova feedback, but with a uniform ionizing background, as in [Ramsøy et al. \(2021\)](#), also develop temperature envelopes around gas filaments.

Perspectives

In the remaining stages of this internship, several promising avenues for further exploration have been identified. Firstly, the developed methodology can be applied to other regions within the simulation to investigate potential environmental differences compared to the region studied during this internship. Secondly, the analysis can be expanded to include additional properties such as gas velocity, providing a more comprehensive understanding of the evolution of inter-galactic filaments through the Epoch of Reionization (EoR). Moreover, complementing my analysis with also a halo-centric approach could yield valuable insights into the filament-halo relationship. For instance, focusing on the suppression of star formation in galactic halos and examining whether this suppression, or "quenching", is influenced by the properties of the connected filaments could be of interest for understanding dwarf galaxy evolution.

Bibliography

- Aubert, D. & Teyssier, R. 2008, *Mon. Not. R. Astron. Soc.*, 387, 295
- Aubert, D. & Teyssier, R. 2010, *The Astrophysical Journal*, 724, 244
- Birnboim, Y. & Dekel, A. 2003, Racah Institute of Physics, The Hebrew University, Jerusalem, Israel
- Bond, J. R., Kofman, L., & Pogosyan, D. 1996, *Nature*, 380, 603
- Collaboration, P. 2014, *Astronomy Astrophysics*, 571, A16
- Danovich, M., Dekel, A., Hahn, O., & Teyssier, R. 2012, Racah Institute of Physics, The Hebrew University, Jerusalem 91904, Israel
- Deparis, N., Aubert, D., Ocvirk, P., Chardin, J., & Lewis, J. 2019, *Astronomy & Astrophysics*, 622, A142
- Dubois, Y. & Teyssier, R. 2007, Service d'Astrophysique, CEA/DSM/DAPNIA/SAp, Centre d'Études de Saclay, L'Orme des Merisiers, 91191 Gif-sur-Yvette Cedex, France
- Edelsbrunner, H. & Harer, J. L. 2010, *Computational Topology* (Providence, RI: American Mathematical Society)
- Elias, L. M., Genel, S., Sternberg, A., et al. 2020, *Monthly Notices of the Royal Astronomical Society*, 494, 5439
- Forman, R. 2002, *A user's guide to discrete Morse theory*
- Gallego, S. G., Cantalupo, S., Lilly, S., et al. 2018, *Monthly Notices of the Royal Astronomical Society*, 475, 3854
- Giavalisco, M., Vanzella, E., Salimbeni, S., et al. 2011, *The Astrophysical Journal*, 743, 95
- Gnedin, N. Y. 2016, *The Astrophysical Journal*, 833, 66
- Guy, J., Bailey, S., Kremin, A., et al. 2023, *The Astronomical Journal*, 165, 144
- Gyulassy, A. 2009, PhD thesis, University of California, Berkeley
- Japelj, J., Laigle, C., Puech, M., et al. 2019, *Astronomy & Astrophysics*, 632, A94
- Kacprzak, G. G., Churchill, C. W., & Nielsen, N. M. 2012, *The Astrophysical Journal Letters*, 760, L7
- Kereš, D., Katz, N., Weinberg, D. H., & Davé, R. 2018, *Astronomy Department, University of Massachusetts at Amherst, MA 01003*
- Kikuta, S., Matsuda, Y., Cen, R., et al. 2019, *Publications of the Astronomical Society of Japan*
- Kimm, T., Devriendt, J., Slyz, A., et al. 2018, *Monthly Notices of the Royal Astronomical Society*
- Kooistra, R., Silva, M. B., Zaroubi, S., et al. 2019, *Monthly Notices of the Royal Astronomical Society*, 490, 1415
- Lee, K.-G., Hennawi, J. F., White, M., Croft, R. A. C., & Ozbek, M. 2014, *The Astrophysical Journal*, 788, 49

- Levermore, C. D. 1984, Journal of Quantitative Spectroscopy and Radiative Transfer, 31, 149
- Lewis, J. S. W., Ocvirk, P., Dubois, Y., et al. 2022, Observatoire Astronomique de Strasbourg, Universite de Strasbourg, CNRS UMR 7550, 11 rue de l'Universite, F-67000 Strasbourg, France
- Martin, D. C., Matuszewski, M., Morrissey, P., et al. 2016, The Astrophysical Journal Letters, 824, L5
- Ocvirk, P., Aubert, D., Chardin, J., Deparis, N., & Lewis, J. 2019, Astronomy & Astrophysics, 626, A77
- Ocvirk, P., Aubert, D., Sorce, J. G., et al. 2020, CNRS, Observatoire astronomique de Strasbourg, Universite de Strasbourg, UMR 7550, F-67000 Strasbourg, France
- Ocvirk, P., Gillet, N., Shapiro, P. R., et al. 2016, Observatoire Astronomique de Strasbourg, Universite de Strasbourg, CNRS UMR 7550, 11 rue de l'Universit e, F-67000 Strasbourg, France
- Ocvirk, P., Lewis, J. S. W., Gillet, N., et al. 2021, Observatoire Astronomique de Strasbourg, Universite de Strasbourg, CNRS UMR 7550, 11 rue de l'Universit e, F-67000 Strasbourg, France
- Ocvirk, P., Pichon, C., & Teyssier, R. 2018, Astrophysikalisches Institut Potsdam, An der Sternwarte 16, D-14482 Potsdam, Germany
- Ostriker, J. 1964, Yerkes Observatory, Williams Bay, Wisconsin
- Pichon, C., Pogosyan, D., Kimm, T., et al. 2011, Institut d'Astrophysique de Paris, 98 bis boulevard Arago, 75014 Paris, France
- Pogosyan, D., Bond, J. R., Kofman, L., & Wadsley, J. 1998, in Wide Field Surveys in Cosmology, ed. S. Colombi, Y. Mellier, & B. Raban (Paris: Frontieres), 61
- Powell, L. C., Slyz, A., & Devriendt, J. 2011, Service d'Astrophysique, CEA-Saclay, Orme des Merisiers, 91191 Gif-sur-Yvette Cedex, France and Oxford Astrophysics, Denys Wilkinson Building, Keble Road, Oxford OX1 3RH and Universite Claude Bernard Lyon I, CNRS UMR 5574, ENS-L, Observatoire de Lyon, 9 Avenue Charles Andr e, 69561 St-Genis-Laval Cedex, France
- Rams y, M., Slyz, A., Devriendt, J., Laigle, C., & Dubois, Y. 2021, Sub-department of Astrophysics, University of Oxford, Keble Road, Oxford OX1 3RH, UK and Sorbonne Universites, CNRS, UMR 7095, Institut d'Astrophysique de Paris, 98 bis bd Arago, F-75014 Paris, France
- Ribaudo, J., Lehner, N., Howk, J. C., et al. 2011, The Astrophysical Journal, 743, 207
- Sorce, J. G., Gottl ber, S., Yepes, G., et al. 2016, Monthly Notices of the Royal Astronomical Society, 455
- Sousbie, T. 2011, Monthly Notices of the Royal Astronomical Society, 414, 350
- Sousbie, T., Pichon, C., & Kawahara, H. 2011, Monthly Notices of the Royal Astronomical Society, 414, 384
- Stanway, E. R. & Eldridge, J. J. 2018, Department of Physics, University of Warwick, Gibbet Hill Road, Coventry CV4 7AL, UK
- Stewart, K. R., Brooks, A. M., Bullock, J. S., et al. 2013, The Astrophysical Journal, 769, 74
- Teyssier, R. 2002, Astronomy & Astrophysics, 385, 337
- Umehata, H., Fumagalli, M., Smail, I., et al. 2019, Science, 366, 97
- York, D. G., Adelman, J., Jr., J. E. A., et al. 2000, The Astronomical Journal, 120, 1579
- Zomorodian, A. J. 2009, Cambridge Monographs on Applied and Computational Mathematics, Vol. 16, Topology for Computing (Cambridge: Cambridge University Press)